In: AIAA SciTech Forum 2023, 23-27 January 2023, National Harbor, Maryland
DOI: 10.2514/6.2023-1005

Upstream Turbulence Effects on the Self-Similarity of Wakes: Vortex Pair Dynamics

Prasanth K Murari*, Anderson R. Proença† and Kevin P. Garry‡
School of Aerospace, Transport and Manufacturing, Cranfield University, Cranfield, MK43 0AL, United Kingdom

A pair of counter-rotating vortices is a very common flow feature associated with aircraft and ground vehicles. This paper details the research conducted by the authors to understand the effect of upstream turbulence on a pair of counter-rotating vortices generated using a slender delta wing model with a 76° leading-edge sweep. The level of upstream turbulence is predicted to have an effect on the spatial development and decay of such vortices, which is crucial to determine safe or optimal separation distances in aerospace, automotive and motorsport applications. CFD simulations were performed for four different angles of attack (10°, 15°, 20° and 25°) by employing RANS as well as DDES turbulence modeling approaches. Wind Tunnel testing was performed by utilising passive turbulence-generating grids. Unsteady, three-dimensional velocity data is recorded for three wake locations using a 4-hole cobra probe. Self-similarity analysis of mean velocity profiles has been performed for the near-wake region to quantify the effect of turbulence on vortex characteristics. The vortices were observed to retain their functional profile even in high turbulence conditions until the three-dimensional instabilities came into play. However, increasing turbulence reduced the strength (circulation) of the vortices and amplified the three-dimensional instabilities that led to the eventual decay of the pair. The findings of this research can be further evaluated to see if a viable flow control technique can be devised to accelerate the decay of undesirable trailing vortices.

I. Nomenclature

AOA	=	Angle of Attack
CAD	=	Computer-Aided Design
CFD	=	Computational Fluid Dynamics
CFL	=	Courant–Friedrichs–Lewy
DDES	=	Delayed Detached-Eddy Simulation
DNS	=	Direct Numerical Simulation
FST	=	Freestream Turbulence
LES	=	Large-Eddy Simulation
LEV	=	Leading Edge Vortex
RANS	=	Reynolds-Averaged Navier-Stokes

II. Introduction

In fluid dynamics, the term vortex is associated with the phenomenon in which the fluid rotates around a common axis. The strength of the vortex is quantified by its vorticity, a measure of the rate of local fluid rotation. The most commonly observed fluid flows, like the transitional and the turbulent ones, are characterised by local fluid rotation due to viscous effects, leading to the generation of eddies and vortices. Such vortical flows are inherently complex and exhibit rich fluid phenomena, and hence have been of interest to researchers for several decades: [1].

The vortices of interest for this project are the ones commonly encountered in aeronautical applications. Leading-Edge Vortices (LEVs) generated through unconventional wing planforms like the Delta Wing augment the lift generation, help achieve much higher stall angles and improve the manoeuvrability of the aircraft. In most modern aircraft, vortex

*MSc Aerospace Dynamics, Cranfield University
†Research Fellow in Experimental Aerodynamics, Applied Aerodynamics Group, AIAA Member.
‡Professor of Experimental Aerodynamics, Applied Aerodynamics Group,AIAA Member.

Published by AIAA. This is the Author Accepted Manuscript issued with: Creative Commons Attribution Non-Commercial License (CC:BY:NC 4.0).
The final published version (version of record) is available online at DOI:10.2514/6.2023-1005. Please refer to any applicable publisher terms of use.

generators are used as flow control devices to delay the boundary layer separation and improve aerodynamic performance. Vortex generators are also common in the automotive and motorsport sectors due to flow control applications. However, the generation of vortices can be involuntary and undesirable. One such widely known phenomenon is the generation of wing tip vortices from an aircraft. The 'spillage' around the wing tips leads to a loss of aerodynamic performance, and the downwash creates a local induced angle of attack that leads to additional induced drag. These vortices often extend several body lengths into the wake when shed from the wings. The vortex wake formed as a result poses a potential danger to the following aircraft. In most of these applications, the aircraft experiences some form of Freestream Turbulence (FST). Turbulent flows are rotational (non-zero vorticity), diffusive (rapid mixing and increased rates of momentum, heat, and mass transfer) and dissipative (kinetic energy gets converted into heat due to viscous shear stresses). Hence, one could guess that turbulence has the potential to significantly alter the spatial development of these trailing vortices: [2].

A pair of counter-rotating vortices, one of the elementary configurations considered in the literature, closely resembles these trailing vortices. Despite the conceptual simplicity, a vortex pair can exhibit very complex aerodynamic features, including 2D rotation, merging with smaller vortices or three-dimensional instabilities. Understanding the role of turbulence in spatial evolution and subsequent decay of such vortex pairs has the potential to provide useful insights about safe and optimal separation distances: [3]. In this research, an existing 76-degree slender Delta wing model was used to generate a pair of counter-rotating vortices and perform turbulence studies. The model can be visualised in Figure 1. It has a chord length of 300mm and was machined out of a 3mm thick steel plate.

Fig. 1 76-degree Delta wing model

Although the authors appreciate the significance of smaller scales of turbulence and cascade process in wake recovery and overall flow development, the scope of this research was limited to the effects of changing statistically averaged parameters like Turbulence Intensity and Integral Length Scales owing to computational, experimental and time constraints. The wind tunnel testing was done using passive turbulence-generating grids and simpler flow measurement instrumentation to reduce the setup time. The quantitative self-similarity studies were restricted to the near wake region owing to the highly complex and transient flow physics in the far wake. However, any observed far-wake transient features were qualitatively assessed.

The objectives of the research were defined as follows

1) Perform numerical simulations for flow over the chosen delta wing model using ANSYS Fluent
2) Obtain the effect of upstream turbulence (specifically turbulence intensity) on the self-similarity of velocity profiles in the near wake for four different angles of attack
3) Predict the far wake effects using transient CFD analysis
4) Perform wind tunnel testing to evaluate the capability of CFD to accurately predict these turbulence effects

Section III of the report details the literature review performed to understand existing developments in the fields of vortex dynamics, delta wing aerodynamics and self-similarity in vertical flows, thus paving a way to emphasise areas where further research is needed. Section IV presents the computational methodology and procedures adopted to solve the problem. Section V provides details of the wind tunnel facilities, experimental setup, instrumentation and other procedures adopted to perform validation for computational studies. The details of upstream flow characterisation are

detailed in Section VI, and the flow visualisation results from CFD are detailed in Section VII. Self-Similarity analysis of both the computational and experimental data is detailed in Section VIII. Section IX gives a summary and conclusion of the report.

III. Literature Background

A. Self-similarity in Free Shear Flows

For developing turbulent free shear flows, it has been observed that although the mean velocities and other mean quantities change with distance downstream, they often retain the same functional forms. This phenomenon occurs when the problem lacks a characteristic length or time scale. Equation 1 shows a general expression proposed by A. A. Townsend to assess self-similarity in a developing turbulent free shear flow: [4]. The variation of a mean quantity, M, must be of the form.

$$M = M_1 + M_0[f_n(y/l_0, z/l_0)] \tag{1}$$

where, y and z represent the transverse directions' coordinates (x being the streamwise direction), M_1 is the reference mean quantity, M_0 is the mean quantity scale, and l_0 is the length scale. An additional condition is that these constants are only a function of x, the streamwise location. The most commonly used scaling parameters in self-similarity studies are centreline velocity deficit (for M_0) and wake half-width (for l_0).

B. Delta Wing Aerodynamics

When a delta wing is set at a high enough incidence to the oncoming flow, the flow separates at the sharp leading edges and curls into a vortex sheet above the wing, forming two strong counter-rotating vortices. The vortices grow in size and strength as they travel downstream as vorticity is continuously fed along the leading edge. Depending on the angle of attack of the wing and Reynolds number, two of the factors that influence the strength of the primary vortices, a lateral adverse pressure gradient could be created. This results in the flow separating again at the secondary separation line, forming a secondary vortex. The secondary vortex may lead to yet another adverse pressure gradient resulting in the formation of a tertiary vortex: [5–7]. The general anatomy of flow over a delta wing at a high angle of attack can be visualised in Figure 2.

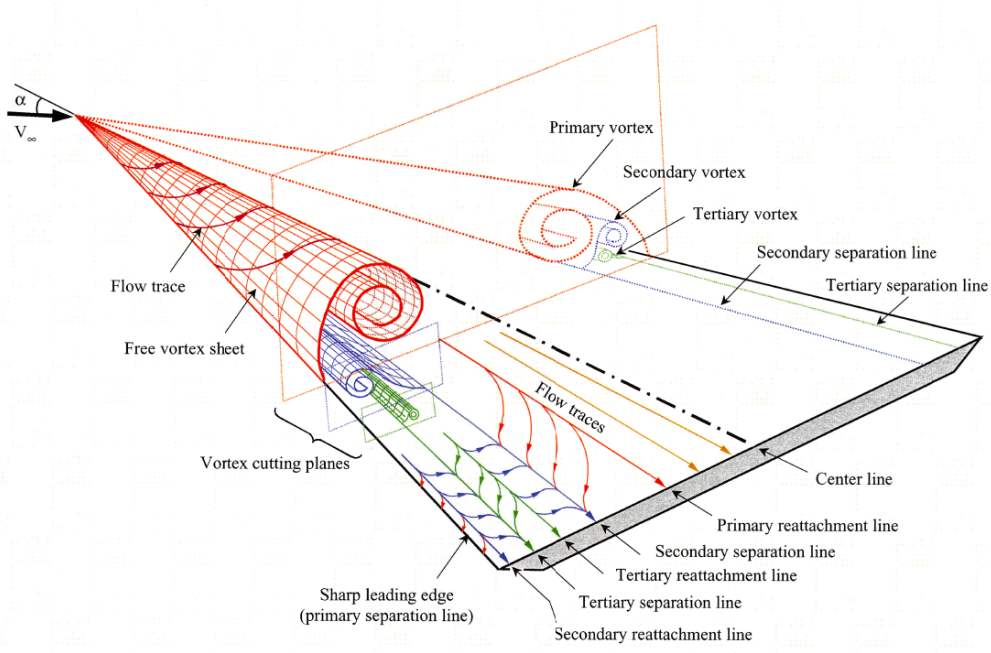

Fig. 2 Anatomy of vortex flow on a delta wing at high angle of attack [6]

C. Self-similarity in vortex wake

U. Fernández has demonstrated that self-similar behaviour existed for the wake of a vortex generator. The vortex is modelled in polar coordinates using the Batchelor vortex model, which allowed the flow to be described by four parameters: vortex core radius, circulation, convection velocity and helical pitch: [8]. The nature of helical symmetry in vortex flows allows the axial(u_z) and rotational(u_θ) velocities to be linearly related. For the self-similarity analysis, the vortex core radius ($\epsilon(z)$) is taken as the characteristic width of the wake, and velocity scaling is established by the deficit in convection velocity (u_0(z)). Both of these quantities are functions of streamwise coordinate (z). The scaled values of velocity profiles for a fixed axial location can be calculated by the equations 2, 3 and 4.

$$\tilde{u}_z(z, r/\epsilon(z)) = \frac{u_z(z, r/\epsilon(z))}{\max\left[u_z(z, r)\right]} \tag{2}$$

$$\tilde{u}_\theta(z, r/\epsilon(z)) = \frac{u_\theta(z, r/\epsilon(z))}{\max\left[u_\theta(z, r)\right]} \tag{3}$$

$$\tilde{\omega}_z(z, r/\epsilon(z)) = \frac{\omega_z(z, r/\epsilon(z))}{\max\left[\omega_z(z, r)\right]} \tag{4}$$

In flows with low viscous dissipation of the vortex core, a constant value of vortex core diameter can be considered for scaling the length dimension. Figure 3 shows the self-similar profiles obtained by them in their experiment.

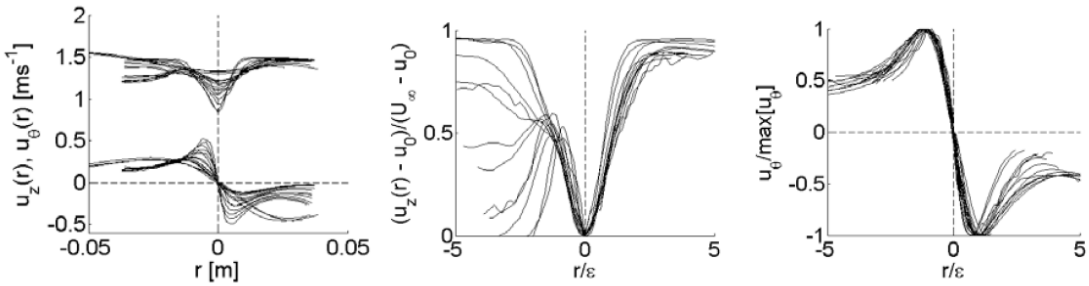

Fig. 3 Development of the axial (u_z) and azimuthal (u_θ) velocity profiles in the wake of the vortex generator and the profiles scaled by self-similarity variables - wind tunnel results [8]

D. Three-dimensional Instabilities

Vortex pairs were found to exhibit quite a few transient phenomena, out of which two mechanisms leading to three-dimensional instabilities are of particular interest in this research: [9].

1. Elliptic Instability

The elliptic instability, which acts to deform the cores, results from a resonance mechanism between two perturbation waves (Kelvin modes) of the underlying axisymmetric structure of each vortex and the modification of this base flow induced by the strain from the other vortex. The external strain produces flow with elliptical streamlines in the vortex core, which has been shown to be three-dimensionally unstable.

2. Crow Instability

This mode of instability is of interest for this project as it is commonly observed with counter-rotating vortex pairs, and it eventually leads to the decay of the pair. During long-wave instability, the vortices undergo sinusoidal deformations, which are symmetric with respect to the centre plane, and they are inclined at an angle of 45° to the line joining the vortices. Eventually, the cores touch and overlap at periodic locations. The vortex re-connection then transforms them into a series of three-dimensional vortex rings.

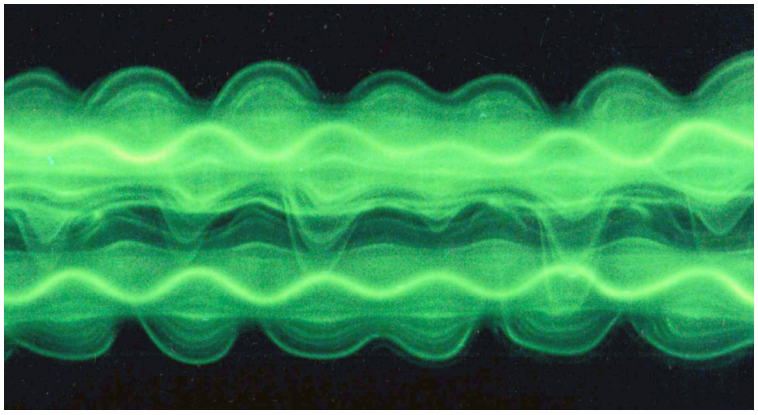

Fig. 4 Water tank dye visualizations of the elliptic instability [10]

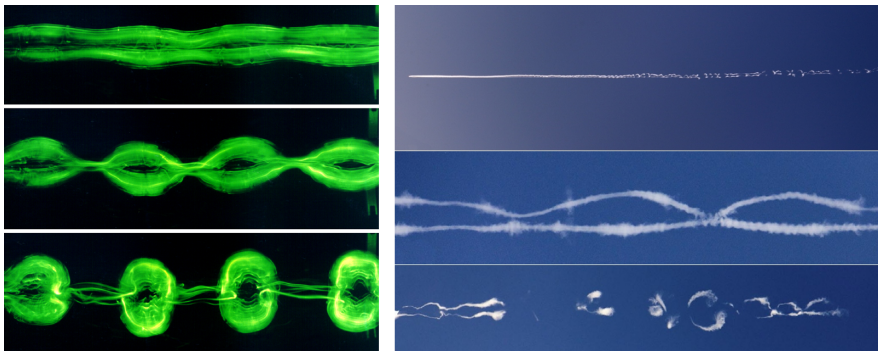

Fig. 5 Long wavelength Crow instability of a counter-rotating vortex pair. Dye visualization in a water tank(left)[11], Jet condensation trails from a Boeing 747 [12]

IV. Computational Methodology

A. Computational Domain

The ANSYS DesignModeler application was used to create the geometry for the computational domain enclosing the Delta wing. The CAD model is imported into the DesignModeler workspace, and a geometry transformation feature is used to set the Angle of Attack (AOA) to the desired value. The domain was extended seven chord lengths in upstream and cross-stream directions and twenty chord lengths in the downstream direction to capture the wake. It was split into three zones (to be referred to hereafter as inner, middle and outer zones) to perform mesh refinement in the vortex wake region. The schematic of the domain and the coordinate system used can be visualised in Figure 7. The origin of the domain is located at the leading edge tip of the wing. Initially, only half the domain was modelled with a symmetry plane to reduce the computational time for steady RANS simulations. The scale and append feature of ANSYS FLUENT solver was used later to create the full domain for unsteady simulations.

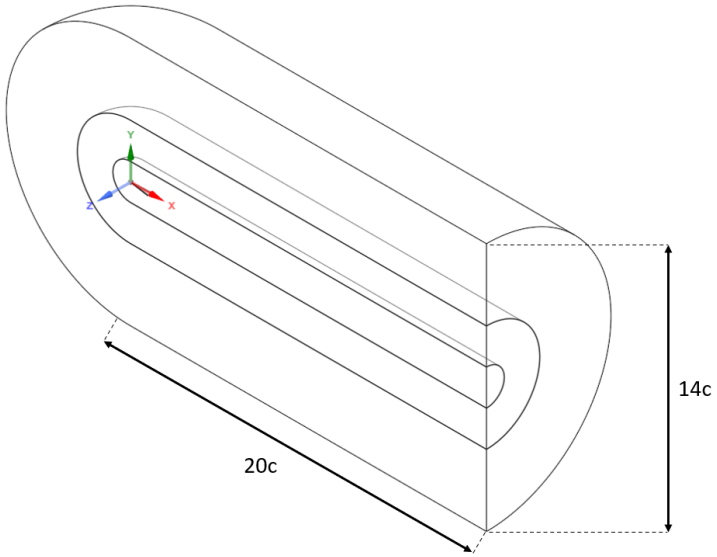

Fig. 6 Schematic of the computational domain used for RANS simulations

B. Mesh Generation

An unstructured mesh methodology was adopted for this research as it offers greater flexibility and ease of discretising the flow domain. It was decided that the k-omega SST turbulence model would be used for the simulations as it provides a better prediction of flow separation than most RANS models and also performs well in flows with adverse pressure gradients. Hence, grid clustering is done close to the wall to ensure y^+ is less than 1.

For a flow velocity of 14 m/s at ISA-standard sea level conditions, the empirical relations for y^+ were worked out, giving $y = 2.4 \times 10^{-5}$m to ensure that y^+ is equal to 1. The inflation layer option of the ANSYS Workbench meshing is used to specify the first layer height. A value of $y = 2.5 \times 10^{-6}$m is set, which ensures the grid can be valid if the boundary conditions are significantly changed in the future. The delta wing model is chosen as the body of influence to gradually increase the size of the cells from the end of the inflation layer into the remaining flow domain. The preliminary mesh generated for the analysis can be seen in Figure 7.

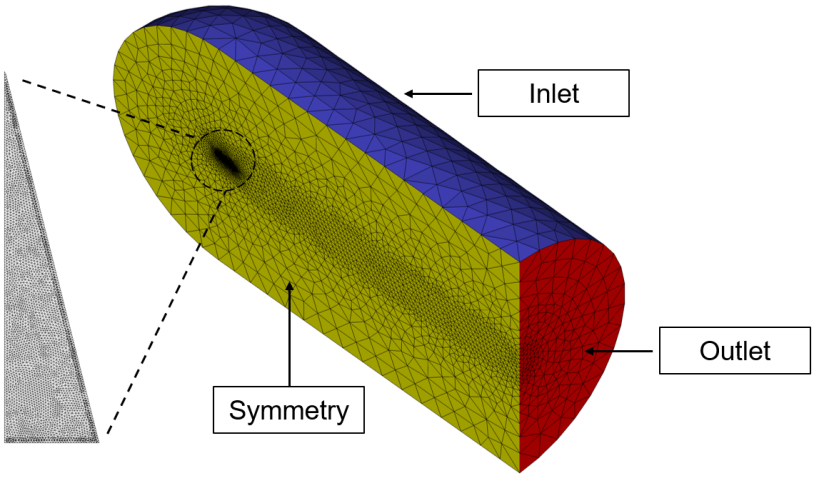

Fig. 7 Preliminary mesh with boundary details

C. Solver Settings

A pressure-based solver was chosen for the simulations since it works well for low-subsonic flows and requires less memory, thus allowing for quicker computation when compared to the density-based solver. A flow velocity of 14 m/s was chosen at ISA standard sea-level conditions for pressure and temperature. A symmetry plane was used to reduce the computation time in RANS simulations.

Pressure-Velocity coupling refers to the numerical schemes which use continuity and momentum equations to derive a relation for pressure correction. SIMPLE, SIMPLEC, PISO, FSM, and Coupled methods are available in FLUENT. SIMPLE, PISO and Coupled algorithms were tested, and it was observed that although the Coupled solver is computationally intensive, it yielded much better convergence. Green-Gauss Node Based discretisation scheme was used to compute gradients of solution variables at cell centres. Although it is more computationally intensive than the Green-Gauss Cell-Based scheme, it minimises false diffusion and is more suitable for unstructured meshes. Since a tetrahedral meshing method was used(flow not always aligned with the grid), all the field variables are interpolated with the Second-Order Upwind scheme.

For the DDES simulations, a synthetic turbulence generator was used along with the same Intensity and Length Scale values used in RANS. The transient formulation was set to Bounded Second Order Implicit and Momentum discretization to Bounded Central Differencing as required by the turbulence model.

D. Mesh and Time Step Sensitivity Analysis

Before starting the RANS simulations, mesh sensitivity analysis was performed to ensure that the solutions obtained had minimal spatial discretization errors and that the chosen mesh size was optimal. Five different meshes were tested with an increasing number of elements, as shown in Fig 8.

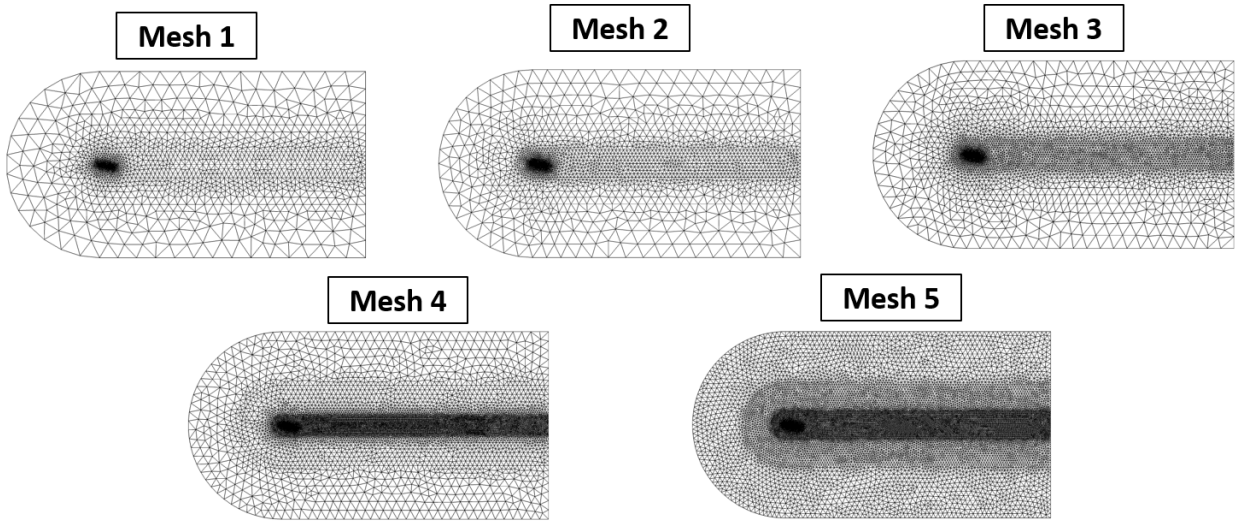

Fig. 8 Symmetry-plane view of meshes used for sensitivity analysis for AOA = 10°

The dependence of the Lift coefficient (C_L), Drag coefficient (C_D) and the Pitching Moment Coefficient (C_M) on the size of the mesh can be observed in figure 9. Hence, Mesh 3 was chosen to perform further simulations for AOA = 10° cases. A similar analysis was performed for the three remaining angles. Mesh 3 was also chosen for AOA = 15° cases, whereas Mesh 4 was chosen for AOA = 20° and 25° cases.

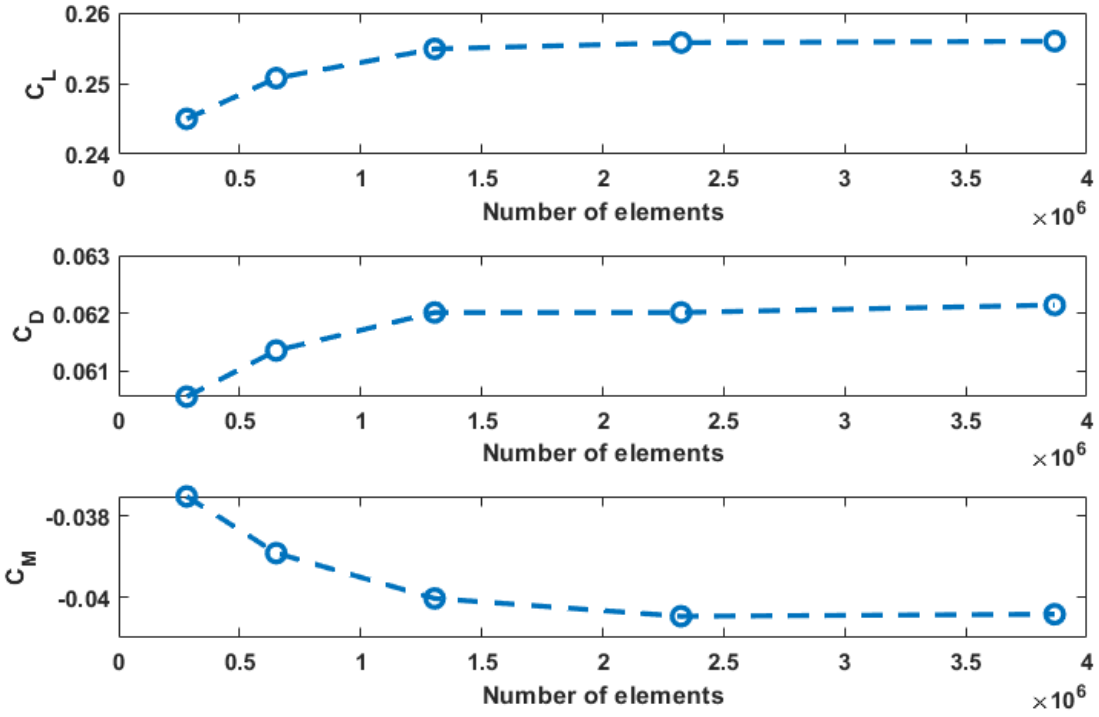

Fig. 9 Dependence of force and pitching moment coefficients on the size of the mesh for AOA = 10°

Similar to spatial discretization errors, transient simulations will have additional errors due to temporal discretization. It is critical to choose the time step so that all the necessary oscillating flow mechanisms are captured by the solution. The preliminary choice for the time step can usually be made either through a literature review of frequencies associated with vortex shedding or by choosing a value such that the CFL number is less than 1 in the LES regions. Table 1 details several unsteady flow phenomena associated with wings and their respective Strouhal numbers.

Phenomenon	Strouhal Number
Helical Mode Instability	1-2
Shear Layer Instabilities	8 -10 and higher frequencies
Vortex Shedding -Trailing edge	8
Vortex Shedding -high Angle of Attack	0.2 -0.5
Vortex Breakdown Oscillation	0.01 -0.08

Table 1 Frequencies corresponding to important unsteady features of vortical flows

To ensure that the CFL number is less than 1 for the chosen mesh and the flow conditions, the time step needs to be set to 0.00017 seconds, which means that about 500 core hours were needed per test case. Even with a High-Performance Computer, this was undesirable. Fast Fourier Transform (FFT) analysis is performed on the time histories of force coefficients and pressure recording at four probe locations as an alternative method. Three time steps (0.004 seconds, 0.002 seconds and 0.001 seconds) were tested with the highest angle of attack, i.e. 25°. C_L, C_D and C_M time histories were recorded along with static pressure and total velocity values for the probe locations mentioned in table 2 and visualised in 10.

Probe number	x	y	z
1	150	-40	-25
2	300	-75	-50
3	450	-90	-50
4	600	-100	-50

Table 2 Location of probes(in mm) for time step analysis for DDES

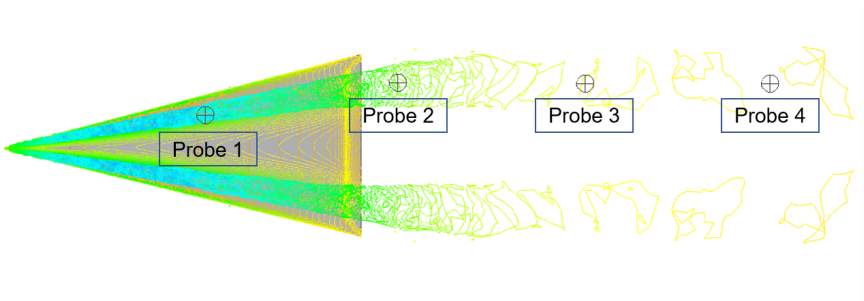

Fig. 10 Visualisation of the location of probes in relation to vortex

The obtained C_L time histories for the last one second of the flow (after statistical steadiness is reached) can be seen in Figure 11. Based on these plots and the FFT plots, a time step of 0.002 seconds was chosen for the simulations.

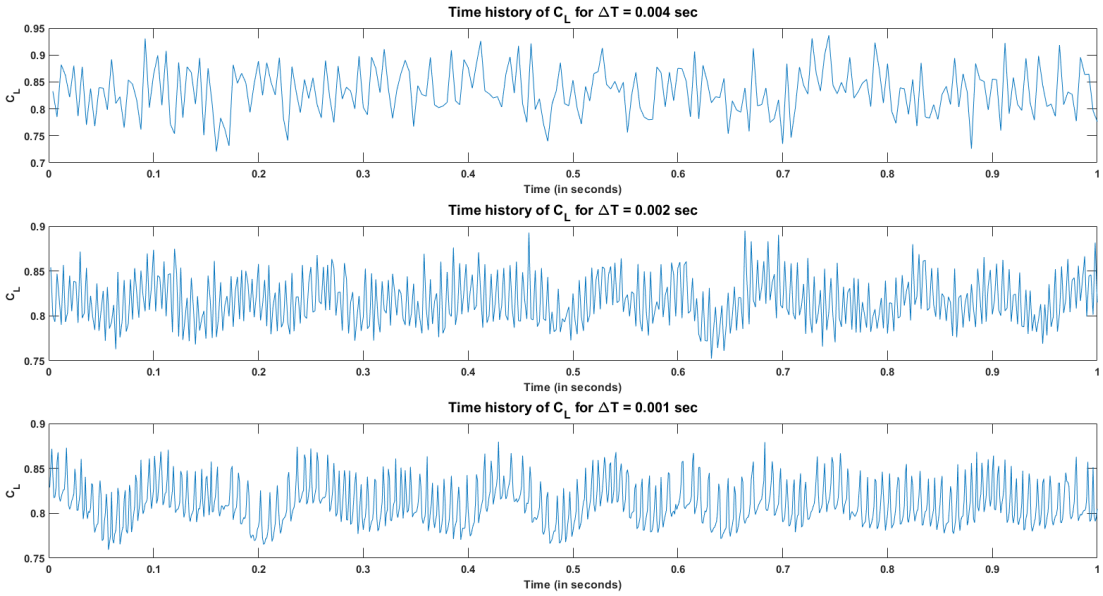

Fig. 11 Time histories of C_L for different time steps using DDES

E. Test Cases

A total of 40 cases were tested by changing the inlet turbulence intensity for four different angles of attack with both RANS and DES. The details of conducted CFD test runs are given in table 3.

Turbulence model	AOA(°)	Inlet TI(%)	Inlet Length Scale(mm)
RANS	10, 15, 20, 25	0.5, 1, 2, 5, 10, 20, 30	10
DDES	10, 15, 20, 25	2, 5, 10	10

Table 3 Details of CFD test cases

The RANS simulations were done for 20000 iterations each until the residuals were sufficiently converged. The DDES simulations were done for a total flow time of 2.5 seconds, with 80 iterations per time step. The first second of the flow is done using a coarse time step of 0.01 seconds to accelerate the RANS calculation when turbulence boundary conditions are changed. It was let to settle for one more second with a time step of 0.002 seconds, and the velocity data for the last half second was recorded for analysis. The solution data was written for five downstream locations, x = 0.6m, 0.75m, 0.9m, 1.05m and 1.2m, which correspond to 2, 2.5, 3, 3.5 and 4 chord lengths downstream of the leading edge tip. The y-coordinates for which the line data was written are given in Table 4.

AOA(°)	x = 600mm	x = 750mm	x = 900mm	x = 1050mm	x = 1200mm
10	-40	-45	-52	-60	-67
15	-80	-88	-95	-105	-120
20	-112	-122	-140	-155	-173
25	-145	-167	-200	-215	-235

Table 4 y-coordinates (in mm) of lines for which solution data is recorded in CFD

V. Experimental Methodology

A. Experimental setup

The experiments for this project were conducted in the Donnington wind tunnel facility at Cranfield University. It is an open return suction-type subsonic wind tunnel with a 0.9 m^2 working section and a maximum flow velocity of 30 m/s. The small working section of the wind tunnel contributes to a relatively higher freestream turbulence intensity of 0.3% to 0.5% in the test section. The experimental model was mounted in the test section using a single-strut mounting system with a hinge, as shown in Figure 12. This kind of mechanism minimises the flow blockage and interference with Leading Edge Vortices.

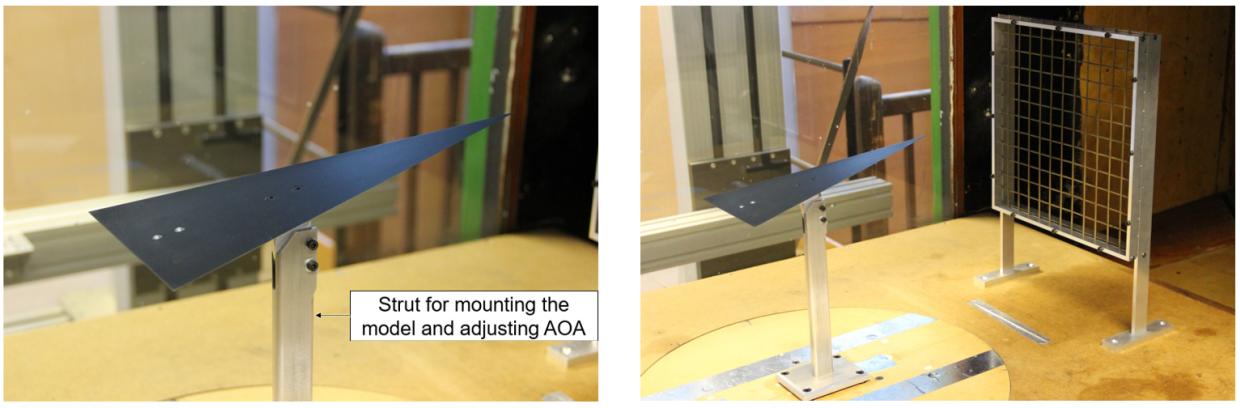

Fig. 12 Model and turbulence grid setup in the test section

A reference coordinate system was chosen for the experiment in which the origin lies on the centreline of the working section, on the ground at the streamwise location corresponding to the leading edge tip of the wing(when AOA = 0°). Like the coordinate system used in CFD, the streamwise direction is set as positive x and vertically upwards as positive y. Hence, the positive z direction is away from the viewer as per the right-hand rule.

The maximum recommended bluff-body blockage ratio for the tunnel is about 11.5%. Hence, the size of the turbulence-generating grids was set to 312mm x 312mm. A frame was made to hold the grids and mounted upstream of the model. The centre of the frame's base lies at x = -360mm. Three different grids, named the Wire grid, Bar grid and Fractal grid, were used to generate different levels of turbulence in the tunnel. The final arrangement of the test model and the upstream grid assembly containing the wire grid can be viewed in Figure 12 on the right. The geometry of the other two grids can be viewed in Figure 13. These two grids were milled out of aluminium plates.

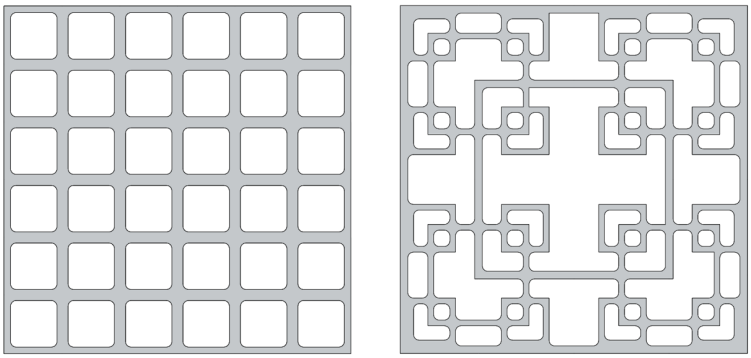

Fig. 13 CAD models of Bar grid(left) and Fractal grid(right)

B. Flow Measurement Instrumentation

The velocity measurements in the wake of the model were performed using a TFI Series 100 Cobra Probe. The Cobra Probe is a 4-hole pressure probe that provides dynamic 3-component velocity and local static pressure measurements in real-time. The Probe is capable of a linear frequency response from 0 Hz to more than 2 kHz and is available in various ranges for use between 2 m/s and 100 m/s. It can measure flow angles in a ±45° cone, all six Reynolds stresses and allows calculation of other higher-order terms: [13].

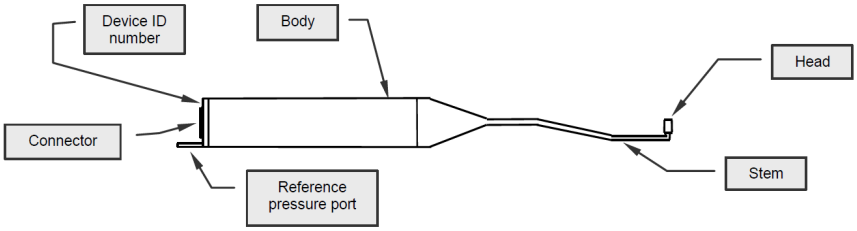

Fig. 14 Series 100 Cobra Probe main features [13]

The data acquisition was performed using the *TFI Device Control* software. For each data point, the total acquisition time is set to 30 seconds at a sampling rate of 5 kHz. Table 5 provides the details of the other measurement instruments used in the experiment.

Measurement type	Instrument type	Instrument Model
Ambient temperature	Thermometer	RS 408-6165
Ambient pressure	Barometer	Omega HHP360
Dynamic pressure	Differential Pressure transducer	FCO 318
Angle of attack	Protractor	PRO 360 Digital protractor
Distance	Ruler	Standard ruler

Table 5 List of measurement instruments used in the experiment

C. Traverse details

The Cobra Probe was mounted on a traverse system that allowed movement in the cross-stream plane. The system consists of two vertical posts and a horizontal post on the top, with screw thread slides in each of the posts. A stepper motor was used to drive the horizontal screw thread slide. The National Instruments MID-7604 integrated stepper motor power drive was used to control the traverse from a desktop computer.

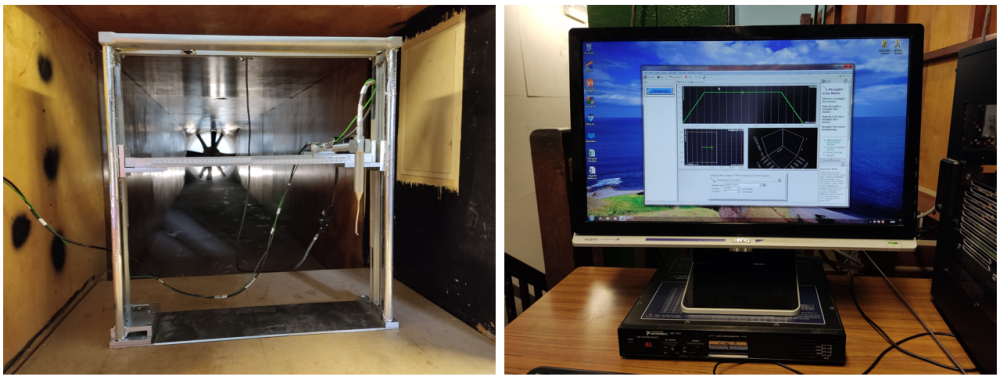

Fig. 15 Images showing setup (left) and control computer(right) of traverse

Unfortunately, control of the traverse in the vertical direction was not possible due to hardware limitations. The belt connecting the vertical thread slides was moved manually to adjust the vertical position of the probe between different test runs. The traverse also had inconsistencies while moving horizontally. A pointer was attached to the cobra probe mount to overcome the problem and monitor the movement, and a printed scale with 1mm divisions was stuck on the traverse.

D. Test Procedure

The test procedure involved recording transient velocity data for three downstream locations. The tests were performed for four angles of attack (10°, 15°, 20° and 25°). Based on available testing time and instrumentation issues, recording velocity data for full planes downstream of the model was impossible. Hence, it was decided that data acquisition would be made on lines passing through the vortex. The vortex core's approximate height(location) from the ground for different angles of attack and downstream locations was determined using a tuft wand and cobra probe measurements as shown in Figure 7. The indication of the probe lying on the line joining the vortices is the high pitch angle of the flow as the probe approaches the vortex, whereas a high yaw angle indicates that the probe is located close to either top or bottom edges of the vortex core. The tuft wand was used to get a rough location, and the probe was used to make fine adjustments. The velocity profiles were recorded at three downstream locations for four different angles of attack under four different turbulence conditions, resulting in a total of 48 runs for self-similarity analysis. Two repeat runs were conducted to check for the repeatability of the test and to perform uncertainty analysis.

The table 7 details the vertical coordinates of locations chosen for each downstream location and each AOA to record the velocity data. In all the test runs for self-similarity analysis, the traverse is moved in the z-direction starting from $z = -10mm$ to $z = +90mm$ in steps of 5mm each, and further till $z = +130mm$ in steps of 10mm each.

Angle of Attack	x = 600mm	x = 750mm	x = 900mm
10°	280mm	272.5mm	265mm
15°	260mm	250mm	235mm
20°	240mm	220mm	205mm
25°	215mm	210mm	175mm

Table 6 Approximate height of vortex core from the ground plane

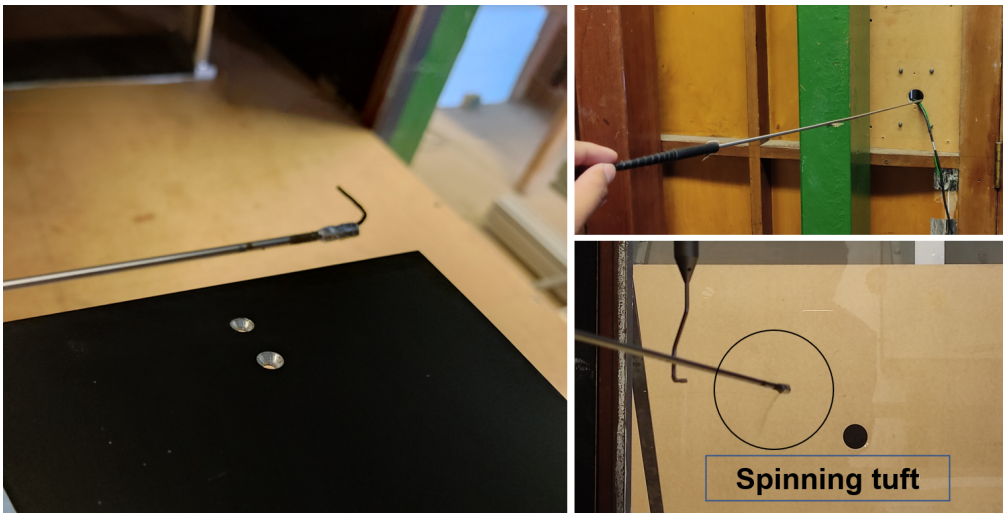

Fig. 16 Images depicting use of tuft wand through an access hole in the working section to spot the vortex core

A non-uniform velocity profile in the test section meant that the differential pressure transducer cannot be used to determine velocity ahead of the delta wing; the test velocities were set by taking the point lying on the centreline ($z = 0$) for $x = 600mm$ as a reference. For the $x = 750mm$ and $x = 900mm$ runs, the throttle is matched with similar configurations of $x = 600mm$ runs. This, however, doesn't ensure exactly the same velocity since the blockage effects change depending on the traverse location. Hence, this experiment cannot accurately predict the evolution of the axial velocity of the vortex core.

Three additional runs were performed in which the velocity profiles downstream of the turbulence grids were measured without the test model. In these runs, the distance between the grid frame and the cobra probe was set to 360mm, the same distance between the frame and wing in previous runs. Fairly large steps were taken using traverse due to time constraints. Although the regions of measurement were small, the entire area where the model lies for all angles of attack was covered. The regions mapped in this process are as shown in Figure 17.

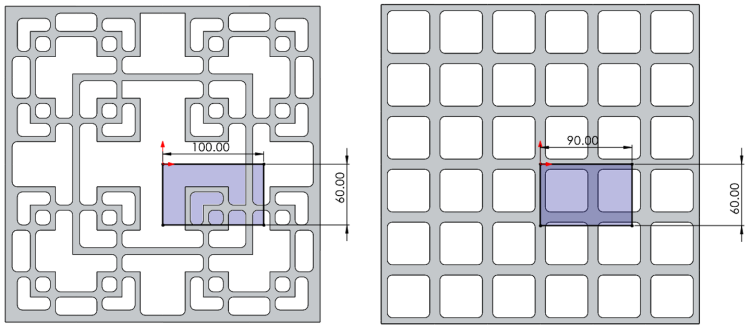

Fig. 17 Image showing the sketch of regions where flow measurements are taken behind the Bar and Fractal grids

Grid name	y positions(mm)	z positions(mm)
Fractal Grid	220, 240, 260, 280	0 to 100 (10mm steps)
Bar Grid	220, 240, 260, 280	0 to 90 (15mm steps)
Wire Grid	240, 260, 280	0 to 90 (15mm steps)

Table 7 y and z coordinates of the grids in which velocity measurements were done downstream of turbulence grids

VI. Upstream Flow Characterisation

A. CFD upstream flow characterisation

Cross-stream section planes were created for $x = 0m$ to check the contours of turbulence intensity the wing actually experiences. For RANS simulations, the turbulence intensities observed at the geometric origin (coincident with the wing's leading edge tip) are given in Table 8. Figure 18 shows the contours of turbulence intensity on the plane $x = 0$ for two of the RANS cases.

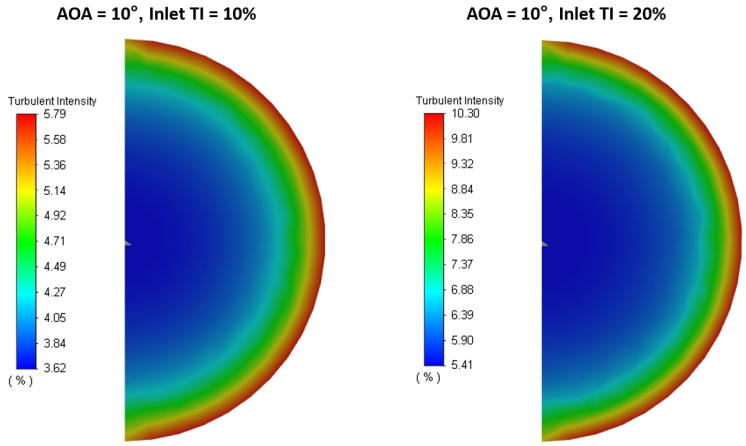

Fig. 18 Contours of Overall TI on the plane $x = 0$ for two of the RANS cases

TI at inlet (%)	0.5	1	2	5	10	20	30
TI at origin (%)	0.33	0.89	1.62	2.29	3.62	5.41	9.41

Table 8 Comparison of turbulence intensities at inlet and origin in RANS simulations

The turbulence intensity contours from DDES were significantly different and non-uniform, and time-varying in nature, as can be seen in Figure 19. It was also observed that dissipation of turbulence intensity was less with the synthetic turbulence generator as compared to RANS turbulence specification.

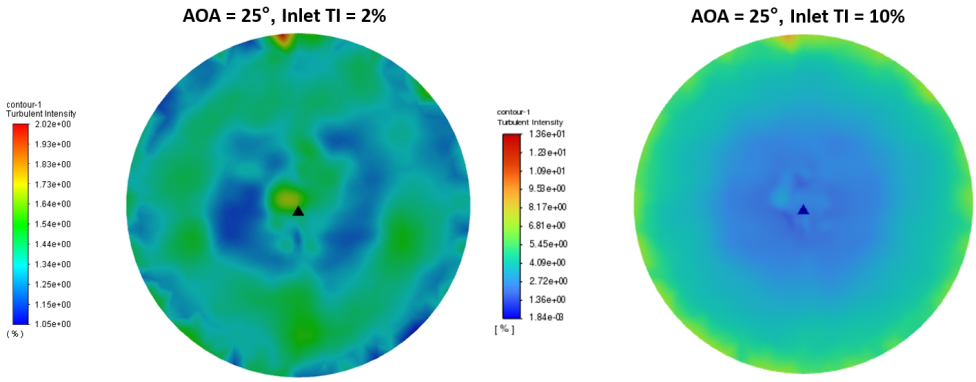

Fig. 19 Contours of Overall TI on the plane $x = 0$ for two DDES cases at $t = 2.5$s

B. Wind Tunnel upstream flow characterisation

The data obtained from the flow mapping done downstream of the turbulence grids was processed to create contours of Overall Turbulence Intensity, and mean velocity was normalised by mean velocity recorded at the centre of the grid($y = 280mm$, $z = 0mm$). Only the overall turbulence intensity contours are presented in this report and can be visualised in Figures 20, 21 and 22. It can be observed from the contour plot and their respective colourbars that the Wire Grid and Bar Grid generated fairly uniform Overall Turbulence Intensity (still non-isotropic with I_{xx} being greater than I_{yy} and I_{zz}). The wire Grid has generated moderate levels of turbulence, whereas the Bar grid generated extremely high levels of turbulence, which is usually found only in turbulent boundary layers and turbo-machinery applications. The fractal grid, however, generated non-uniform levels of turbulence, with minimal turbulence at the centre. The Turbulence Intensity generated by Fractal Grid is lower than that of the Wire Grid at the wing's location, and it increases gradually to higher than Bar Grid's.

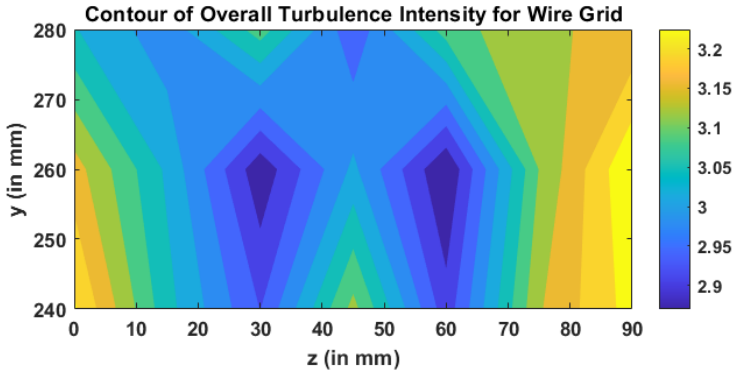

Fig. 20 Contour of Overall Turbulence Intensity for Wire Grid

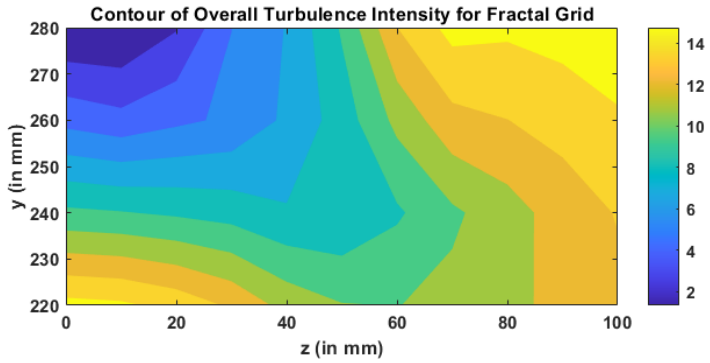

Fig. 21 Contour of Overall Turbulence Intensity for Fractal Grid

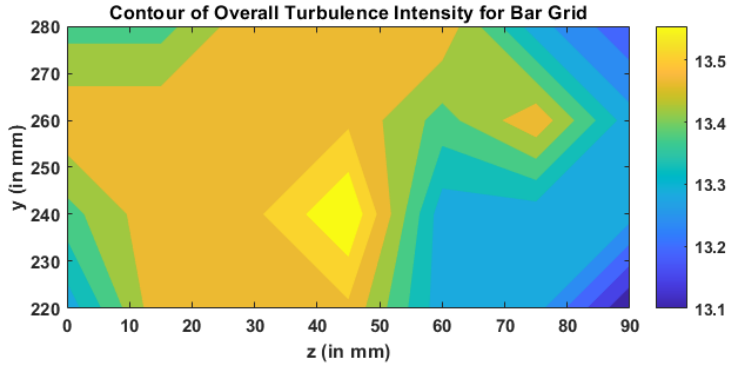

Fig. 22 Contour of Overall Turbulence Intensity for Bar Grid

VII. Flow Visualisation

Isosurfaces of normalised Q-criterion were created for RANS simulations to perform visualisation of the trailing vortices. Figure 23 depicts the static pressure contours on surfaces with normalised Q-criterion = 0.2 for the AOA = 25° case. Static pressure contouring was done to get a qualitative indication of vortex strength which is determined by factors like circulation and axial and angular momentum fluxes. The key observation was that increasing inlet turbulence intensity led to a loss in vortex strength, which also resulted in the secondary vortex not forming. The vortices travel downwards as expected, with the magnitude of travel increasing with increasing AOA. This can be explained by increased shear against the freestream due to stronger vortices for higher angles of attack.

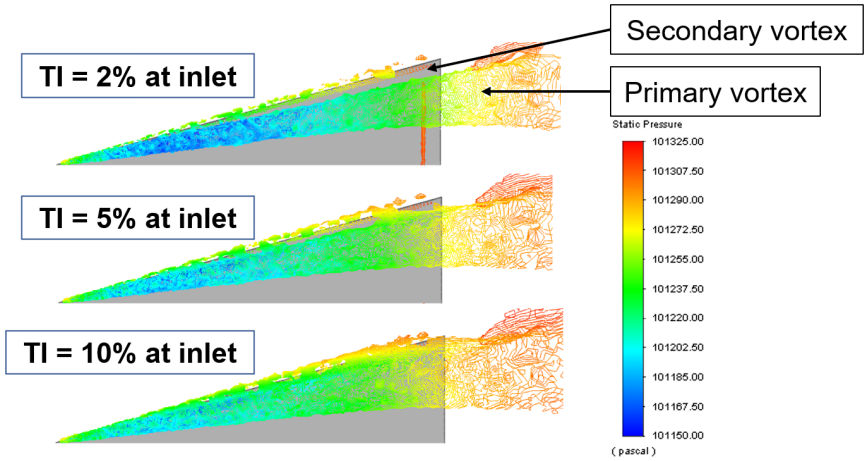

Fig. 23 Isosurfaces of normalised Q criterion (=0.2) for flow over a delta wing at AOA = 25° for three different upstream turbulence conditions

Static pressure contours were made on isosurfaces of Q-criterion (=50) at t = 2.5 seconds for the DDES simulations for different inlet turbulence intensities. The contours for the configuration AOA = 20° are shown in figure 24.

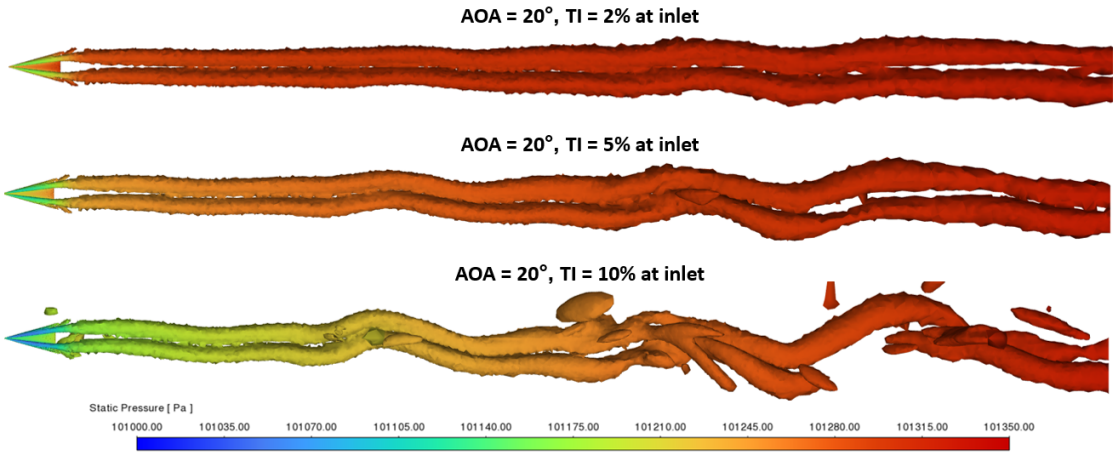

Fig. 24 Static pressure contours on isosurfaces of Q-criterion (=50) for AOA = 20° for three different inlet turbulence intensities using DDES

The phenomenon of long-wave instability is clearly visible. For the lowest inlet turbulence case (2%), significant displacement of vortex cores happens more than twelve chord lengths downstream of the trailing edge. As the turbulence is increased to 5% at the inlet, this distance reduces less than five chord lengths, and the amplitude of long-wave oscillation increases significantly. For the highest turbulence case, the vortex cores touch and start dissociating into discrete regions of vorticity. Hence, it is inferred that increasing turbulence amplifies the long-wave instability of a vortex pair leading to quicker decay of the vortices.

VIII. Self-Similarity Analysis

A. Self-Similarity Analysis of Wind Tunnel data

The self-similarity analysis for the wind tunnel data is restricted to the y-velocity data (vertical cross-stream velocity component). Based on the three-dimensional velocity data, the location of the vortex core (centre) was mapped as shown in Table 9. The results are presented for only one angle of attack.

	x = 600mm	x = 750mm	x = 900mm
No Grid	50	50	52.5
Wire Grid	50	55	55
Fractal Grid	57.5	60	65
Bar Grid	52.5	52.5	57.5

Table 9 z-coordinates (in mm) of vortex core centres obtained from experimental data for AOA = 20°

Since there is a significant movement of the vortex core in most of the runs, the length axis is transformed to have the origin at the predicted vortex core, with the transformed $z - coordinate$ being named z'. This transformation is demonstrated in Figure 25 for one of the test cases. From Figure 25, it is also evident that the y-velocity (to be referred to as v_y hereafter) is influenced by the pitch in the flow. To compare the effect of vortex alone, a new term $v_y{}'$ is computed as shown in equation 5. The resulting velocity transformation is depicted for one case as shown in Figure 26.

$$v_y{}' = v_y + \left| \frac{|max(v_y)| - |min(v_y)|}{2} \right| \tag{5}$$

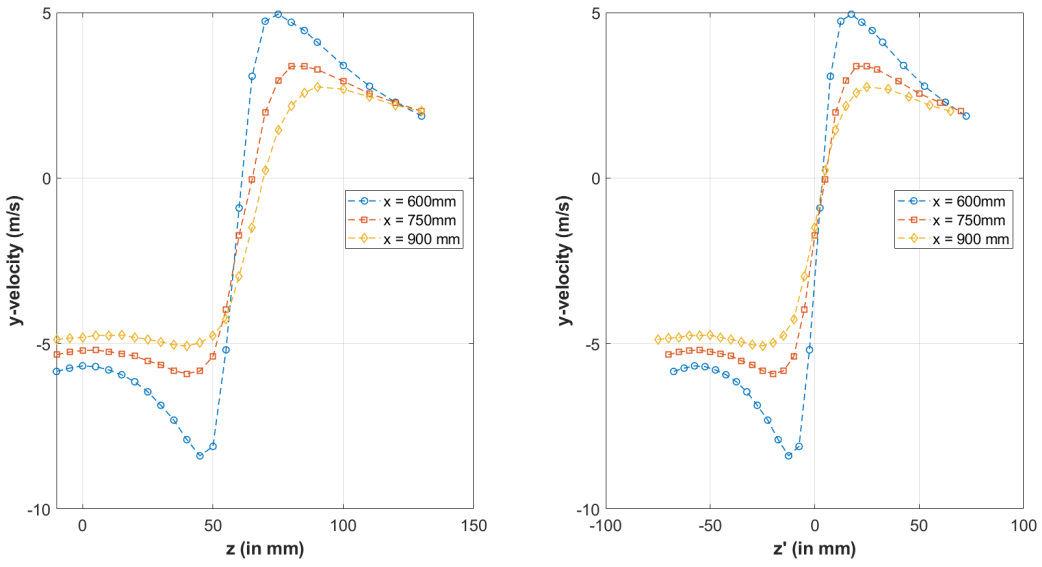

Fig. 25 Plots showing the y-velocity profiles for Fractal Grid AOA = 20° configuration before and after axes transformation

The diameter of the vortex core (ϵ) for each run was nominally taken as the distance between the points with minimum and maximum y-velocities close to the core(like Rankine vortex) or double the distance between the peaks of y-velocity and z-velocity when the former is inconclusive. Finally, the length z' was normalised by vortex core diameter ϵ and the velocity $v_y{}'$ was normalised by $max(v_y{}')$. Figure 27 depicts the collapsed velocity profiles for the Fractal Grid AOA = 20° case.

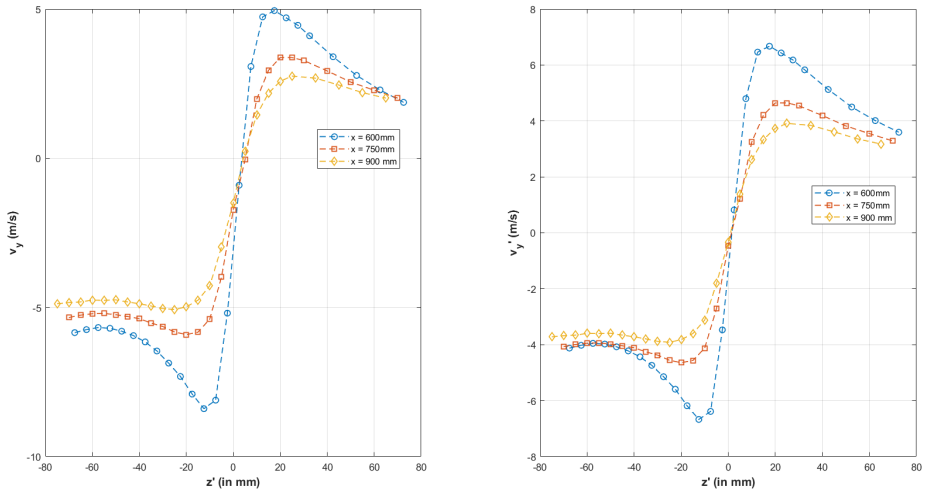

Fig. 26 Plots showing the y-velocity profiles for Fractal Grid AOA = 20° configuration before and after velocity transformation

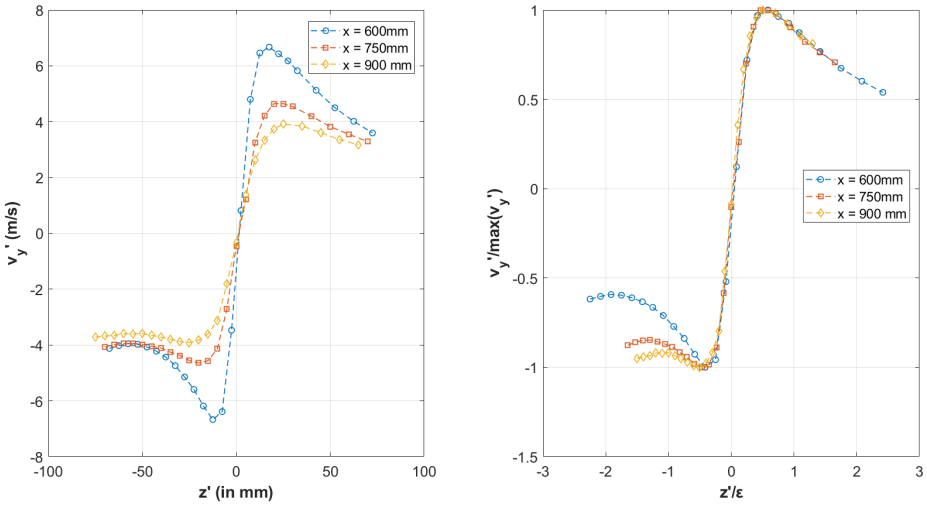

Fig. 27 Plots showing the transformed(left) and collapsed(right) y-velocity profiles for Fractal Grid AOA = 20° configuration

The profiles collapsed greatly for the core, and right side (as seen) of the vortex, whereas the left side of the profiles did not. The preliminary understanding of this phenomenon is the influence of the neighbouring vortex (note that the difference between collapsed profiles is less for the ones downstream). The figures 28 and 29 show the self-similarity plots obtained through similar transformations and normalisation for the two of the other test cases.

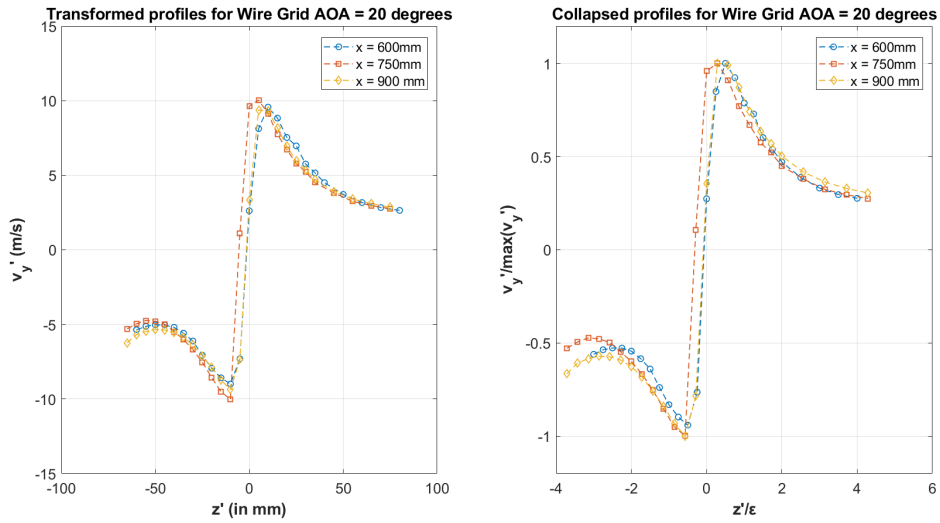

Fig. 28 Plots showing the transformed(left) and collapsed(right) y-velocity profiles for Wire Grid AOA = 20° configuration

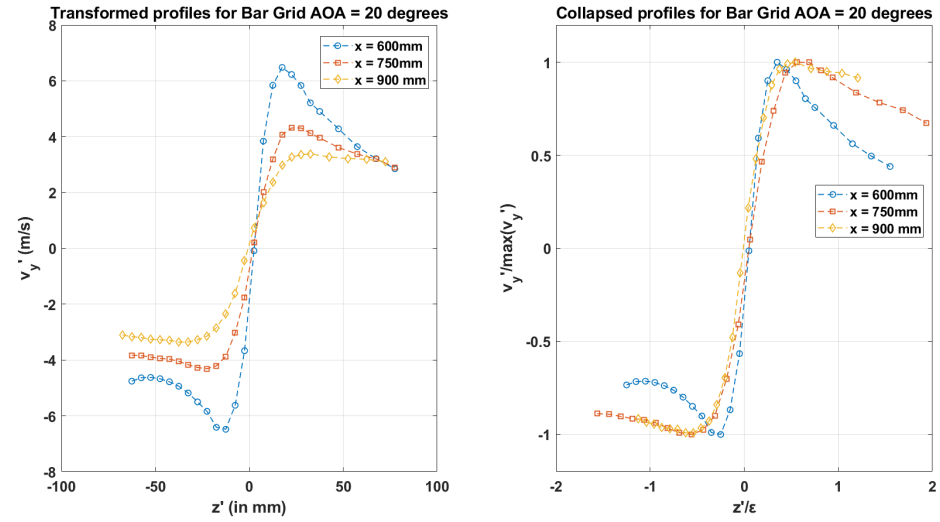

Fig. 29 Plots showing the transformed(left) and collapsed(right) y-velocity profiles for Bar Grid AOA = 20° configuration

It can be observed that increasing turbulence intensity reduced the strength of the vortex, which can be understood by examining the difference between maximum and minimum velocities. This is in agreement with what was predicted using the isosurface contours from CFD. The vortex has retained self-similarity for three of the four cases, with only the Bar Grid self-similarity plot showing a significant deviation from the expected behaviour. However, even for the Bar Grid case, the profiles for $x = 750mm$ and $x = 900mm$ collapse well. Since the same vertical height of measurement is set for all turbulence cases, probe positioning error is an unlikely reason for this to happen. It is predicted that the vortex core has dissipated significantly, thus changing the functional form, or there is a significant oscillation of the vortex leading to flatter average velocity profiles as downstream distance increases. The scaling factors used have worked well for all the cases, thus confirming that the methodology used for the self-similarity of an isolated vortex, as discussed in subsection III.C, can be conveniently applied to a non-isolated vortex.

B. Self-Similarity Analysis of CFD data

For self-similarity analysis of y-velocity profiles obtained from CFD, the y-velocity was transformed similarly to wind tunnel data analysis and normalised by maximum transformed y-velocity. For the x-velocity profiles, self-similarity analysis was done by normalising the velocity deficit with the maximum velocity deficit.

1. RANS Results

Two of the resulting collapsed velocity profiles from RANS simulations are shown in figures 30 and 31. The plots show that the y-velocity profiles collapsed greatly irrespective of the upstream turbulence values, which is not coherent with wind tunnel observations using the Bar Grid. However, the effect of turbulence is visible in the collapsed streamwise velocity profiles.

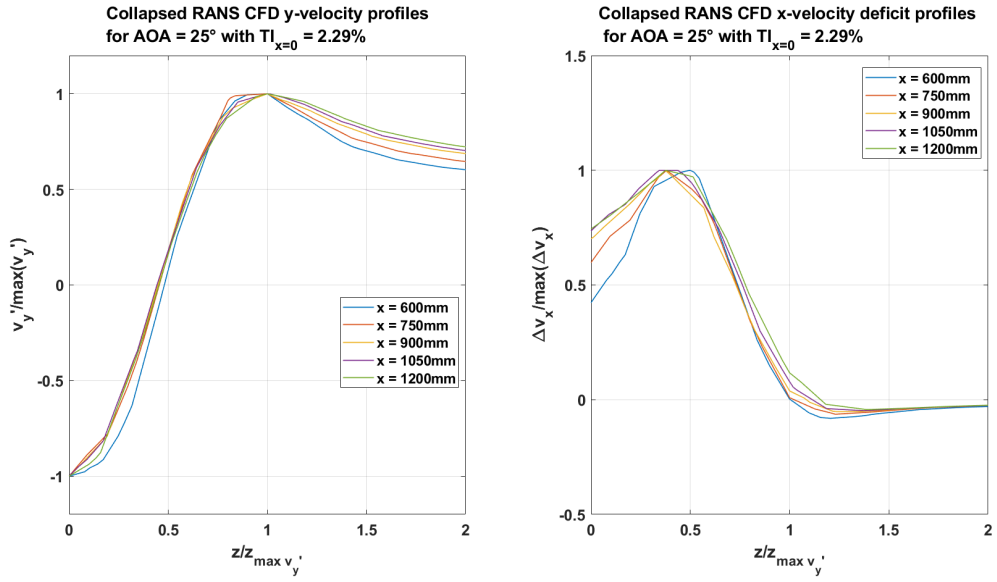

Fig. 30 Collapsed x and y-velocity profiles from RANS CFD for AOA = 25° with $TI_{x=0} = 2.29\%$

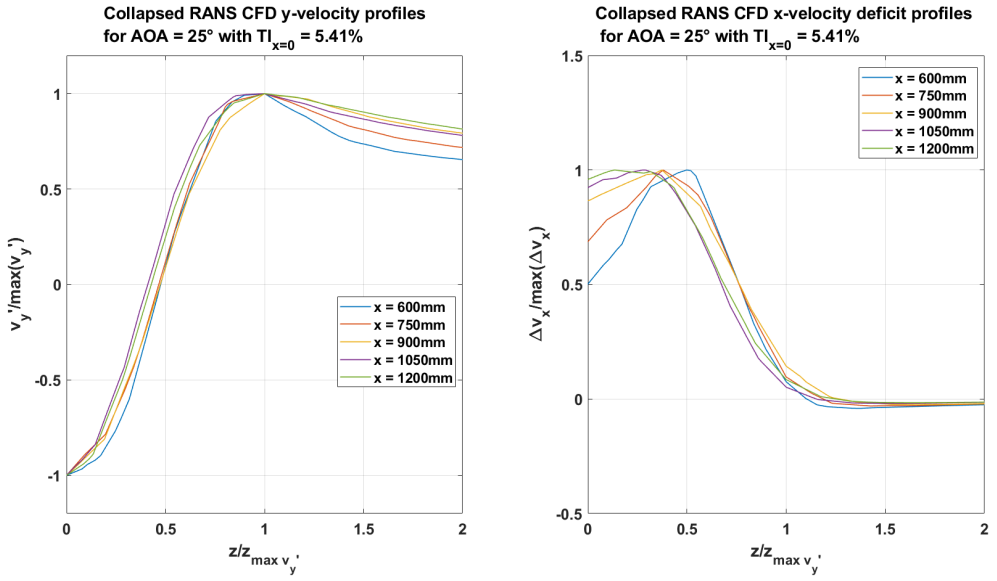

Fig. 31 Collapsed x and y-velocity profiles from RANS CFD for AOA = 25° with $TI_{x=0} = 5.41\%$

Based on the analysis conducted for all the angles of attack, it was observed that increasing turbulence intensity increased the value of $\Delta v_x/max(\Delta v_x)$ on the centerline, which indicates a lesser deficit of streamwise velocity in the core. Deviation from self-similar behaviour is dependent on both the vortex's strength and turbulence intensity values.

2. DDES Results

Unsteady velocity data was recorded during the DDES calculations and then time-averaged during the post-processing to obtain the mean velocity profiles at the same locations. A similar approach to RANS data processing has been adopted. The collapsed velocity profiles for two cases are shown in figures 32 and 33.

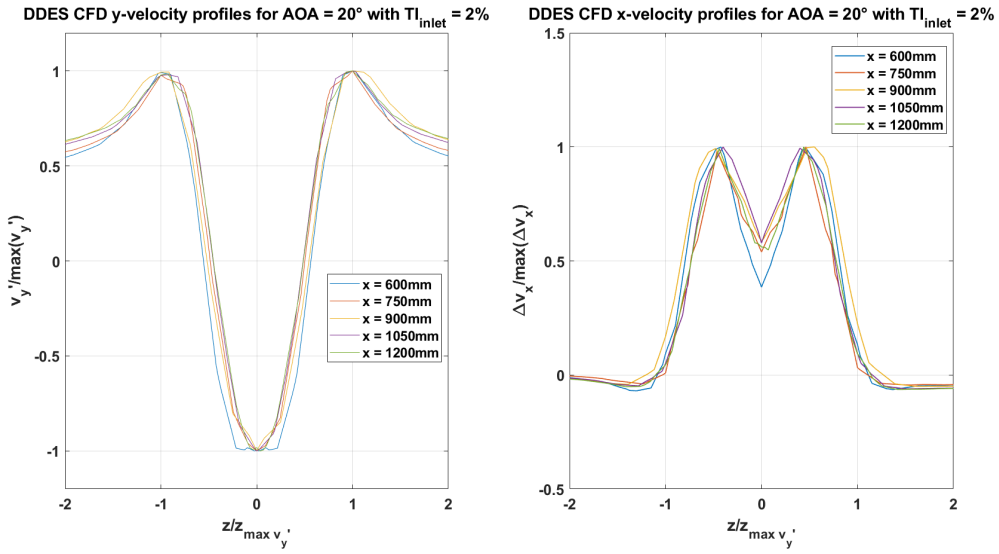

Fig. 32 Collapsed x and y-velocity profiles from RANS CFD for AOA = 20° with $TI_{inlet} = 2\%$

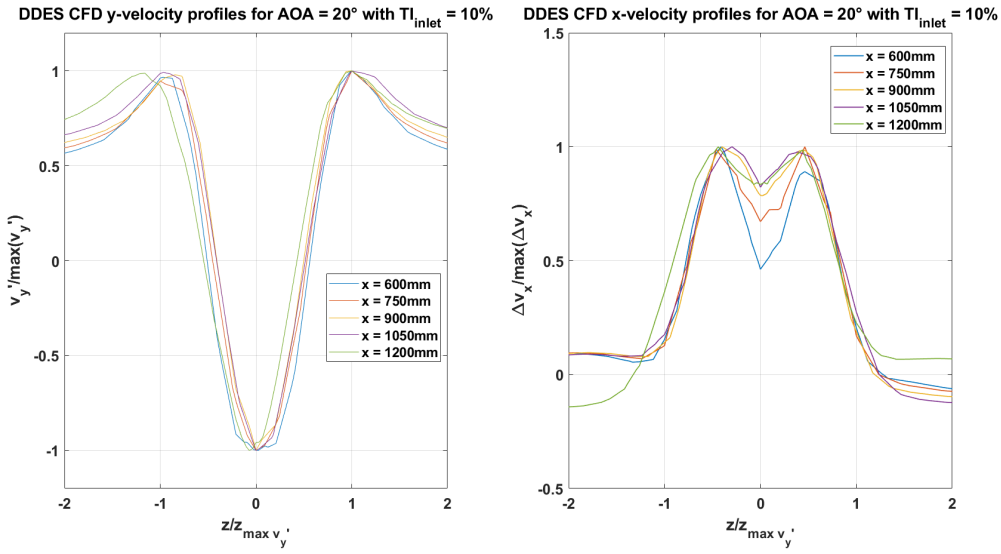

Fig. 33 Collapsed x and y-velocity profiles from RANS CFD for AOA = 20° with $TI_{inlet} = 10\%$

The y-velocity profiles collapse well for low turbulence intensities; however, for the case with the highest turbulence intensity, the profile of the farthest downstream location ($x = 1200mm$) deviates significantly. This is observed for the x-velocity profile as well. This is understood to be the consequence of vortex movement and long-wave oscillation as previously visualised in figure 24.

C. Uncertainty analysis

A few repeat runs were conducted to quantify the uncertainty associated with the cobra probe. However, since the number of data sets is low (=2), it was not possible to derive accurate values of the mean (μ) and standard deviation (σ). For this reason, a t-distribution was used, specifically, a student's t-distribution, since the number of samples is less than 30. The 95% confidence interval can be estimated using Equation 6.

$$\Delta CI = 2|e| = 2|t_{\alpha/2,k}(s^2/n)^{1/2}| \tag{6}$$

where, $t_{\alpha/2,k}$ is dependant on the confidence levels chosen $(1-\alpha)$ and the degrees of freedom ($k = n-1$). The value of k for this case is 1. The value of $t_{\alpha/2,k}$ is equal to 12.71 for a 95% confidence interval with 1 degree of freedom. The plot 34 shows the repeatability error for the y-velocity profiles for Wire Grid AOA = 20° configuration at x = 750mm downstream location. From the plot, it can be observed that the uncertainty of velocity measurement is highest close to the vortex core. This is understood to be primarily due to large velocity gradients in the core and errors associated with the traverse movement.

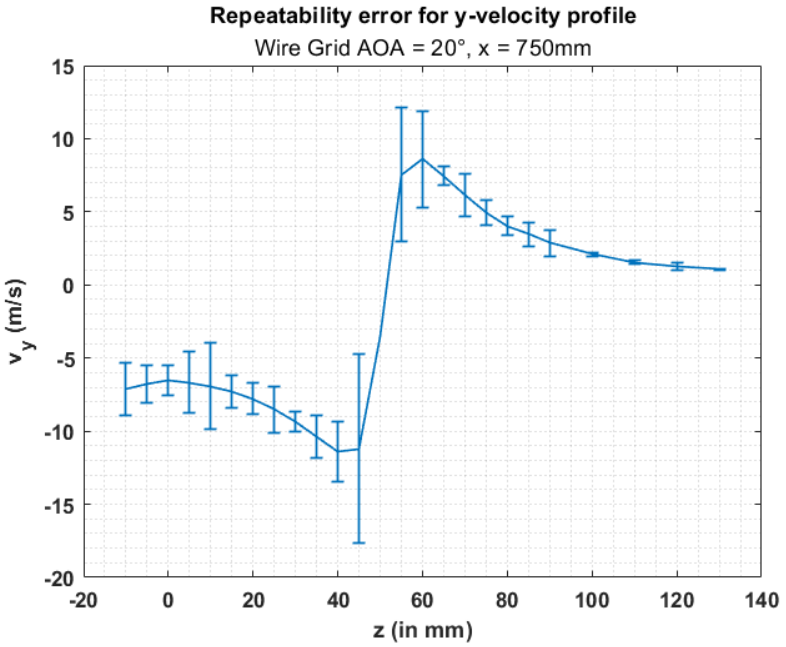

Fig. 34 Uncertainty estimation for y-velocity using student's t-distribution

IX. Conclusion

This research dealt with computational and experimental investigation of the wake of a slender delta wing for different angles of attack and different upstream turbulence conditions. The computational analysis was performed using the k-omega SST turbulence model, and the unsteady simulations were performed using Delayed Detached Eddy Simulation. Mesh sensitivity and time-step sensitivities were performed to get the right trade-off between computational time, costs, and solution accuracy.

The wind tunnel testing was conducted by employing grid-generated turbulence using three different turbulence grids. Flow characterisation and visualisation studies were performed for both the Wind Tunnel and CFD data. The contours showed that the Bar Grid and the Wire Grid generated relatively uniform levels of overall turbulence intensity, whereas the Fractal Grid had a large variation depending on the distance from the centre. The self-similarity analysis of y-velocity was conducted for the experimental results by using the vortex core diameter as the normalising length scale and half of the y-velocity velocity variation across the core as the parameter to normalise y-velocity. The vortex was observed to be self-similar for all downstream locations for the No Grid, Wire Grid and Fractal Grid configurations, which have relatively low levels of free-stream turbulence in the proximity of the wing. A sudden increase in vortex core diameter has been observed for high angles of attack and low freestream turbulence. This was predicted to be due

to vortex breakdown. The uncertainty analysis predicted a large error in y-velocity measurement close to the vortex; hence the recorded values of vortex location and vortex diameter can have large errors.

The computational results with RANS turbulence modeling haven't predicted any change in the functional form of y-velocity profiles or any effects of freestream turbulence on the decay of the vortices. The DDES simulations predicted an earlier decay of the vortex pair in high turbulence conditions due to actual velocity perturbations in the flow field. The self-similarity analysis of the DDES results also showed a deviation from the ideal collapse due to the movement of vortex cores at three chord lengths downstream location. The findings of this research can be further evaluated to see if a viable flow control technique can be devised to accelerate the decay of undesirable trailing vortices.

References

[1] Nitsche, M., "Vortex Dynamics," 2006. URL `https://math.unm.edu/~nitsche/pubs/2006EMP.pdf`.

[2] Tennekes H., L. J., "A First Course in Turbulence," *The MIT Press*, 1972. https://doi.org/10.1146/annurev-fluid-122414-034558.

[3] Leweke, T., Le Dizès, S., and Williamson, C., "Dynamics and Instabilities of Vortex Pairs," *Annual Review of Fluid Mechanics*, Vol. 48, 2016, pp. 507–541. https://doi.org/10.1146/annurev-fluid-122414-034558.

[4] Lighthill, M. J., "The Structure of Turbulent Shear Flow, by A. A. TOWNSEND," *Journal of Fluid Mechanics*, Vol. 1, No. 5, 1956. https://doi.org/10.1017/S0022112056210366.

[5] Anderson, J. D., *Fundamentals of aerodynamics*, sixth edition ed., McGraw-Hill series in aeronautical and aerospace engineering, McGraw Hill Education, New York, NY, 2017.

[6] Pirzadeh, S. Z., "Vortical Flow Prediction Using an Adaptive Unstructured Grid Method," 2003, pp. (SYA) 13–3. URL https://apps.dtic.mil/sti/citations/ADA419029.

[7] Taylor, G., Schnorbus, T., and Gursul, I., "An Investigation of Vortex Flows over Low Sweep Delta Wings," 2003. https://doi.org/10.2514/6.2003-4021.

[8] Fernández, U., Velte, C. M., Réthoré, P.-E., and Sørensen, N. N., "Self-Similarity and helical symmetry in vortex generator flow simulations," *Journal of Physics: Conference Series*, Vol. 555, 2014, p. 012036. https://doi.org/10.1088/1742-6596/555/1/012036, URL https://doi.org/10.1088/1742-6596/555/1/012036.

[9] Leweke, T., Le Dizès, S., and Williamson, C., "Dynamics and Instabilities of Vortex Pairs," *Annual Review of Fluid Mechanics*, Vol. 48, 2016, pp. 507–541. https://doi.org/10.1146/annurev-fluid-122414-034558.

[10] LEWEKE, T., and WILLIAMSON, C. H. K., "Cooperative elliptic instability of a vortex pair," *Journal of Fluid Mechanics*, Vol. 360, 1998, p. 85–119. https://doi.org/10.1017/S0022112097008331.

[11] Leweke, T., and Williamson, C. H. K., "Experiments on long-wavelength instability and reconnection of a vortex pair," *Physics of Fluids*, Vol. 23, No. 2, 2011, p. 024101. https://doi.org/10.1063/1.3531720, URL https://doi.org/10.1063/1.3531720.

[12] Raab, H., "Crow Instability," ???? URL https://epod.usra.edu/blog/2011/08/crow-instability-in-contrails.html.

[13] Ltd, T. F. I. P., "Getting Started Series 100 Cobra Probe," 2015.

https://dspace.org/

Upstream turbulence effects on the self-similarity of wakes: vortex pair dynamics

Murari, Prasanth K.; Proenca, Anderson R.; Garry, Kevin P.

2023-01-19
American Institute of Aeronautics and Astronautics (AIAA)
https://doi.org/10.2514/6.2023-1005
Murari PK, Proenca A, Garry KP. (2023) Upstream turbulence effects on the self-similarity of wakes: vortex pair dynamics. In: AIAA SciTech Forum 2023, 23-27 January 2023, National Harbor, Maryland, USA. Paper number AIAA 2023-1005

Downloaded from a DSpace repository. https://dspace.org/